ARTICLE

DNMT3A^{R882H} accelerates angioimmunoblastic T-cell lymphoma in mice

Jianan Zheng[1,5], Zhongwang Wang[2,5], Xiangyu Pan[1,5], Zhixin Zhang[3], He Li[2], Xintong Deng[1], Pengpeng Liu[1], Qi Zhang[1], Feifei Na[4], Chong Chen[1], Ting Niu[2]✉ and Yu Liu[1]✉

DNA methylation-related genes, including *TET2*, *IDH2*, and *DNMT3A* are highly frequently mutated in angioimmunoblastic T-cell lymphoma (AITL), an aggressive malignancy of T follicular helper (Tfh) cells associated with aberrant immune features. It has been shown that *TET2* loss cooperates with *RHOA*^{G17V} to promote AITL in mice but the functional role of *DNMT3A* mutations in AITL remains unclear. Here, we report that *DNMT3A*^{R882H}, the most common mutation of *DNMT3A* in AITL, accelerates the development of *Tet2*$^{-/-}$; *RHOA*^{G17V} AITL in mice, indicated by the expansion of malignant Tfh cells and aberrant B cells, skin rash, and significantly shortened disease-free survival. To understand the underlying cellular and molecular mechanisms, we performed single-cell transcriptome analyses of lymph nodes of mice transplanted with *Tet2*$^{-/-}$, *Tet2*$^{-/-}$; *RHOA*^{G17V} or *DNMT3A*^{R882H}; *Tet2*$^{-/-}$; *RHOA*^{G17V} hematopoietic stem and progenitor cells. These single-cell landscapes reveal that *DNMT3A* mutation further activates Tfh cells and leads to rapid and terminal differentiation of B cells, probably through enhancing the interacting PD1/PD-L1, ICOS/ICOSL, CD28/CD86, and ICAM1/ITGAL pairs. Our study establishes the functional roles of *DNMT3A* mutation in AITL and sheds light on the molecular mechanisms of this disease.

Oncogene; https://doi.org/10.1038/s41388-023-02699-2

INTRODUCTION

The angioimmunoblastic T-cell lymphoma (AITL) is a subtype of peripheral T-cell lymphoma with malignancy of T follicular helper (Tfh) cells [1]. Unlike other T-cell lymphomas, AITL is a highly inflammatory disease. Clinically, patients with AITL have systemic B symptoms and unique autoimmunity disorders, including rashes, hypergammaglobulinemia, and cytopenia [2, 3]. Histologically, the lymphoma nodes of AITL patients are accompanied by diffused lymphocyte infiltration and high endothelial venule formation [4]. Consistently, malignant Tfh cells are found to be the small population (~10%) in AITL tumors with other numerous tumor environmental cells like histiocytes, epithelioid cells, immunoblasts, eosinophils, and plasma cells [5, 6]. The interaction between Tfh and B cells, likely via costimulatory signaling, including ICOS signaling and CD40 signaling, in the germinal center of AITL directly contributes to the AITL transformation and progression [7, 8]. Besides, PD1, a feature of neoplastic Tfh cells, interacts with PD-L1 in B cells and contributes to AITL-associated high inflammation [9, 10].

Comprehensive genomic landscapes of AITL showed the prevalence of mutations in DNA methylation-related genes like the tet methylcytosine dioxygenase 2 (*TET2*) and DNA methyltransferase 3 A (*DNMT3A*), together with the ras homolog gene family member A (*RHOA*) mutant [11–14]. Loss-of-function mutations of *TET2*, a controller of DNA demethylation by conversion of 5-methylcytosine to 5-hydroxymethylcytosine, is the highest frequently mutated gene that happened in 70–80 % of AITL [11, 12]. It has been demonstrated that loss of *Tet2*, together with *RHOA* hotspot mutant encoding G17V, could drive lymphomagenesis of AITL-like disease in mouse models [7, 15]. Another DNA methylation-related gene *DNMT3A*, in around 30% of AITL samples [11], has been reported as a driving force in other hematopoietic malignancies including acute myeloid leukemia [16, 17]. Of note, *DNMT3A* mutations significantly co-occurred with *TET2* and *RHOA* mutations in AITL patients [13, 18, 19]. It was suggested that the loss of *TET2* and *DNMT3A* may occur early in the hematopoietic stem cells with other mutations such as *RHOA*^{G17V} acquired later in T cells [19, 20]. *DNMT3A*^{R882H}, the most common mutation in AITL, has shown a cooperative effect with *Tet2* loss in promoting mouse acute myeloid leukemia and T-cell lymphoma after a serial bone marrow transplantation [21].

Here, we investigate the impact of *DNMT3A*^{R882H} on *Tet2*$^{-/-}$; *RHOA*^{G17V} AITL formation in mice. With *DNMT3A*^{R882H}, mice developed a skin rash, expansion of Tfh cells, and shorter disease-free survival than the control group. Single-cell RNA-sequence analysis shows further active Tfh cells in the *DNMT3A*^{R882H} AITL sample, leading to B cell differentiation towards memory B cells. Our data highly suggest that *DNMT3A*^{R882H} plays a critical role in driving AITL disease.

[1]Department of Hematology and Institute of Hematology, State Key Laboratory of Biotherapy and Cancer Center, West China Hospital, Sichuan University, Chengdu, China. [2]Department of Hematology, West China Hospital, Sichuan University, Chengdu, China. [3]Department of Technology, Chengdu ExAb Biotechnology, LTD, Chengdu, China. [4]Department of Thoracic Oncology, Cancer Center and State Key Laboratory of Biotherapy, West China Hospital, Sichuan University, Chengdu, China. [5]These authors contributed equally: Jianan Zheng, Zhongwang Wang, Xiangyu Pan. ✉email: niuting@wchscu.cn; yuliuscu@scu.edu.cn

Received: 2 December 2022 Revised: 7 April 2023 Accepted: 18 April 2023
Published online: 01 May 2023

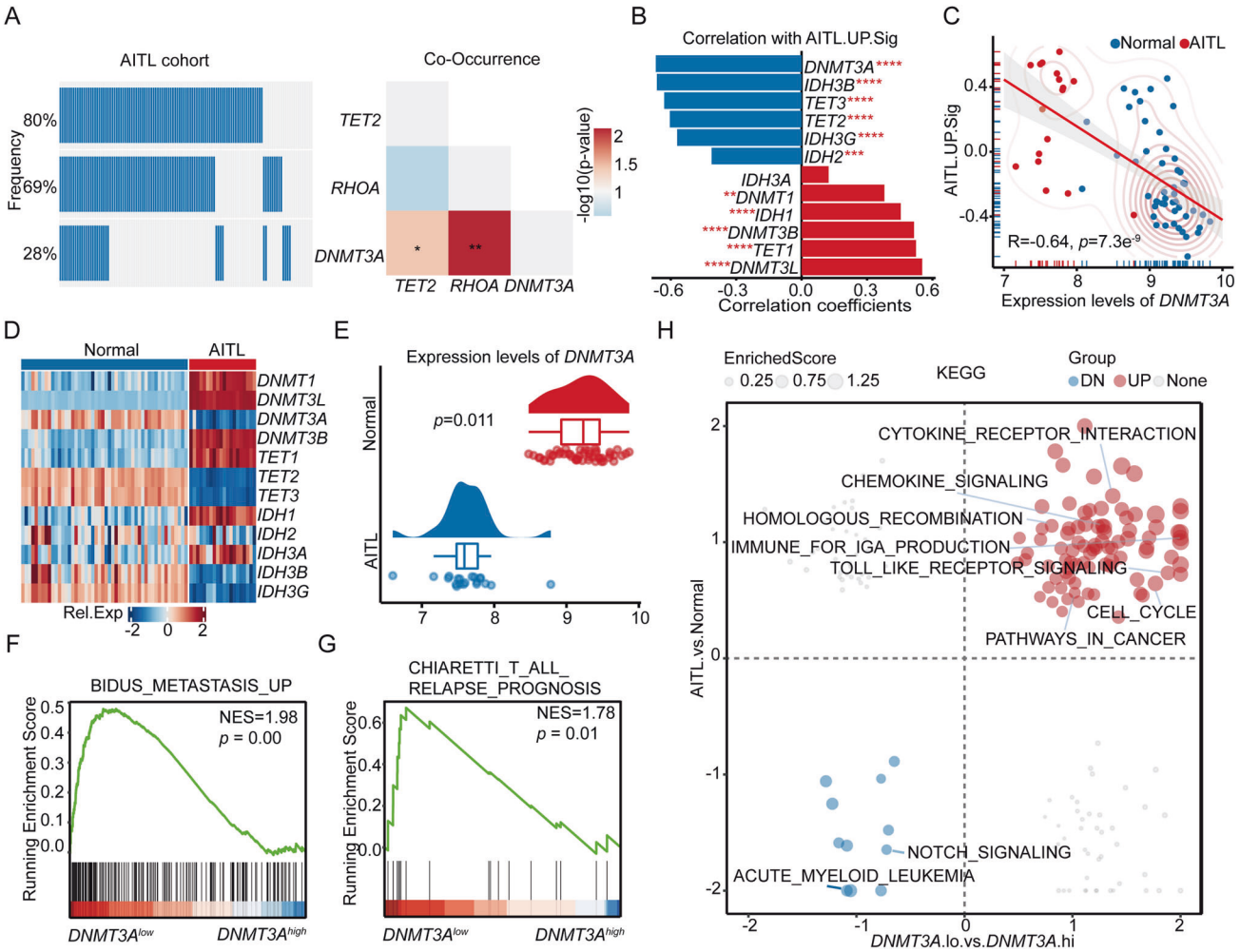

Fig. 1 ***DNMT3A* alterations frequently happen in human AITL. A** The OncoPrint shows the mutation frequencies of *TET2*, *RHOA*, and *DNMT3A* in 117 AITL patients from 3 studies [12, 13, 18]. The heatmap shows the co-occurrences of *TET2*, *RHOA*, and *DNMT3A* mutations. The *p* values summarized the statistic values of co-occurrences between *DNMT3A* and others, the *p* value was calculated by pairwise t-test, $*p < 0.05$, $**p < 0.01$. **B** The bar plot shows the correlation between the expression levels of genes encoding DNA methyltransferase or demethylase and the expressions of AITL.UP signatures in AITL patients. **C** The scatter plot shows the correlation between *DNMT3A* expression levels and the AITL.UP signature in AITL patients or normal cohorts (GTEx). **D** The heatmap shows the expression levels of genes encoding DNA methyltransferases and demethylase in normal or AITL samples from cohort 2. **E** The plot shows the expression levels of *DNMT3A* in normal and AITL samples from cohort 2. **F–G** GSEA showing positive enrichment of BIDUS_METASTASIS_UP and CHIARETTI_T_ALL_RELAPSE_PROGNOSIS signatures in DNMT3A^{low} AITL patients compared to DNMT3A^{high} AITL patients. H. The scatter plot shows the gene set enrichment analysis (GSEA) of KEGG from *DNMT3A*-low verse *DNMT3A*-high AITL patients or AITL patients verse normal samples.

DNMT3A ABNORMALITY IS ASSOCIATED WITH THE AITL SIGNATURE

To investigate the role of *DNMT3A* in human AITL, we analyzed *DNMT3A* mutation frequency, the co-occurrence probability, and expression level in publicly available databases [12, 18, 20, 22]. *DNMT3A* mutations were found in 33 patients (28.21%) among 117 AITL patients (Fig. 1A, Ex. Fig. 1A and Supplementary Table 1), which significantly co-occurred with the alterations of *TET2* and *RHOA* (Fig. 1A and Supplementary Table 2). In addition, we found that the expression levels of *DNMT3A* were negatively significantly correlated with the activity scores of PICCALUGA_ANGIOIMMUNOBLASTIC_LYMPHOMA_UP (AITL_UP.sig) generated from the GSEA database in 20 AITL patients (Fig. 1B and Supplementary Table 3) [6, 22]. As shown in Fig. 1C, data from AITL patients were mostly in the upper left corner representing a lower expression level of *DNMT3A* and higher activation of AITL_UP.sig scores compared with the normal samples (Fig. 1C and Supplementary Table 4). A similar correlation was observed in another AITL cohort (Fig. 1D–E and Ex. Fig. 1C–D) [18]. The AITL patients with lower *DNMT3A* expression (*DNMT3A*^{lo}), compared to those with higher *DNMT3A* expression (*DNMT3A*^{hi}), had significantly higher AITL_UP.sig scores (Ex. Fig. 1B) and enriched metastasis and relapse signature (Fig. 1F–G). Of note, the *DNMT3A*^{lo} AITLs were associated with upregulating chemokine signaling, cytokine receptor interaction, immune for IgA production and cell cycle (Fig. 1H, Ex. Fig. 1E, Supplementary Table 5, and Supplementary Table 6). The notching signaling and acute myeloid leukemia-related pathways were downregulated in *DNMT3A*^{lo} AITLs (Fig. 1H).

DNMT3A^{R882H} ACCELERATES AITL FORMATION IN MICE

To investigate the role of *DNMT3A*^{R882H} in AITL, *Tet2*$^{-/-}$ mouse bone marrow-derived hematopoietic stem and progenitor cells (HSPCs) were transduced with retrovirus-based vectors carrying *RHOA*^{G17V}-IRES-GFP only (*TR*) or together with *DNMT3A*^{R882H}-IRES-mCherry (*TRD*) or empty vector (*Tet2*$^{-/-}$) with comparable

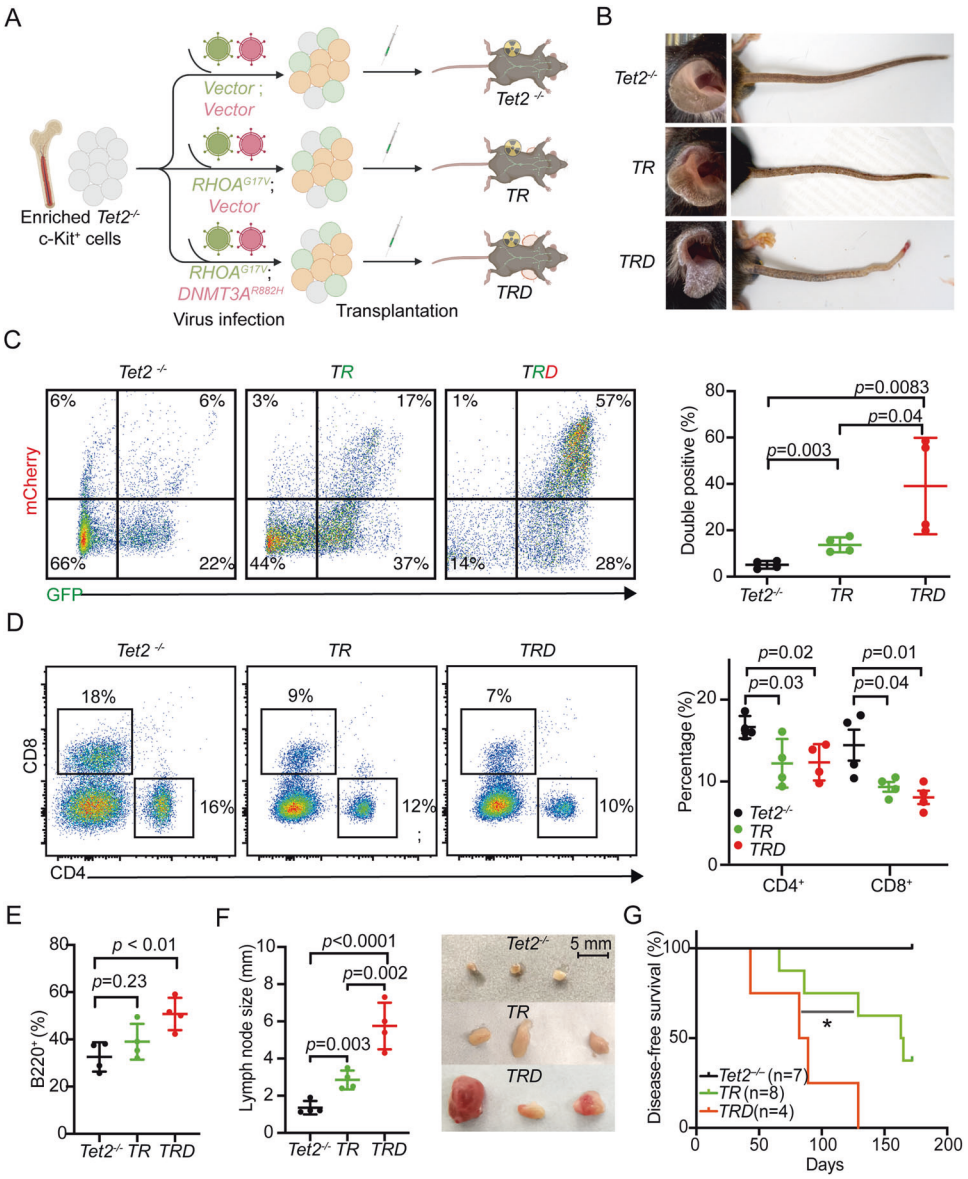

Fig. 2 *DNMT3A*^{R882H} accelerates AITL formation in mice. A Schematic diagram of strategy to generate *Tet2*$^{-/-}$, *TR*, and *TRD* mouse AITL models. **B** Representative images showing the fibrosis of the ears and tail of mice from the *Tet2*$^{-/-}$, *TR*, or *TRD* groups. **C**–**E** Flow cytometry results showing GFP^{+} mCherry^{+}% (**C**), CD4^{+}% or CD8^{+}% (**D**), and B220^{+}% (**E**) in the peripheral blood of the *Tet2*$^{-/-}$, *TR*, and *TRD* groups. The quantitation results (means ± SD, $n = 4$) are shown on the right. *P* values were from the one-way ANOVA *t*-test. **F** Representative images showing the enlarged lymph nodes harvested from the *TR*, and *TRD* groups. Scale bar, 5 mm. Quantitation results represented means ± SD, $n = 4$. Statistics were calculated from a one-way ANOVA *t*-test. **G** Kaplan–Meier disease-free survival of recipient mice transplanted with *Tet2*$^{-/-}$ HSPCs infected with vector (*Tet2*$^{-/-}$), *RHOA*^{G17V} (*TR*) or *RHOA*^{G17V}; *DNMT3A*^{R882H} (*TRD*). ($n = 7$ for *Tet2*$^{-/-}$ group; $n = 8$ for *TR* group, $n = 4$ for *TRD* group, *$p < 0.05$, log-rank test).

infection ratio, followed by bone marrow transplantation into sub-lethally irradiated congenic wildtype recipient mice (Fig. 2A and Ex. Fig. 2A). The *TRD* mice started to show dermatitis phenotypes first in the ears and tails and later to the hair-covered skin 1 month after transplantation, some of which eventually morphed into dorsal skin ulceration (Fig. 2B). Two months after transplantation, the percentage of GFP^{+}mCherry^{+} *TRD* donor cells were significantly enriched in *TRD* mouse peripheral blood, compared to that in *Tet2*$^{-/-}$ and *TR* groups (Fig. 2C). Also, we observed the CD4^{+}% or CD8^{+}% decrease and B220^{+}% increase in *TRD* mice, suggesting aberrant immunological activity (Figs. 2D and 2E). *TR* mice also developed autoimmune syndromes with enlarged lymph nodes, which took much longer time than *TRD* mice (median time: 165 days for *TR* vs 65 days for *TRD*), whereas no recipient *Tet2*$^{-/-}$ mouse had any syndrome in the observation period (Figs. 2F and 2G). These results indicated that *DNMT3A*^{R882H} accelerated AITL formation with aberrant immunoinflammatory phenotypes.

DNMT3A^{R882H} PROMOTES PATHOLOGICAL TFH EXPANSION

We harvested some of the recipient mice after 11-week transplantation. Consistently with our observation in the peripheral blood, lymph nodes from *TRD* mice had more B220^{+} B cells and fewer CD3^{+} T cells compared to that in the other two groups (Fig. 3A). And, CD4^{+} CXCR5^{+} PD-1^{high} Tfh [23] population was significantly increased in *TRD* lymph nodes (Fig. 3B), which

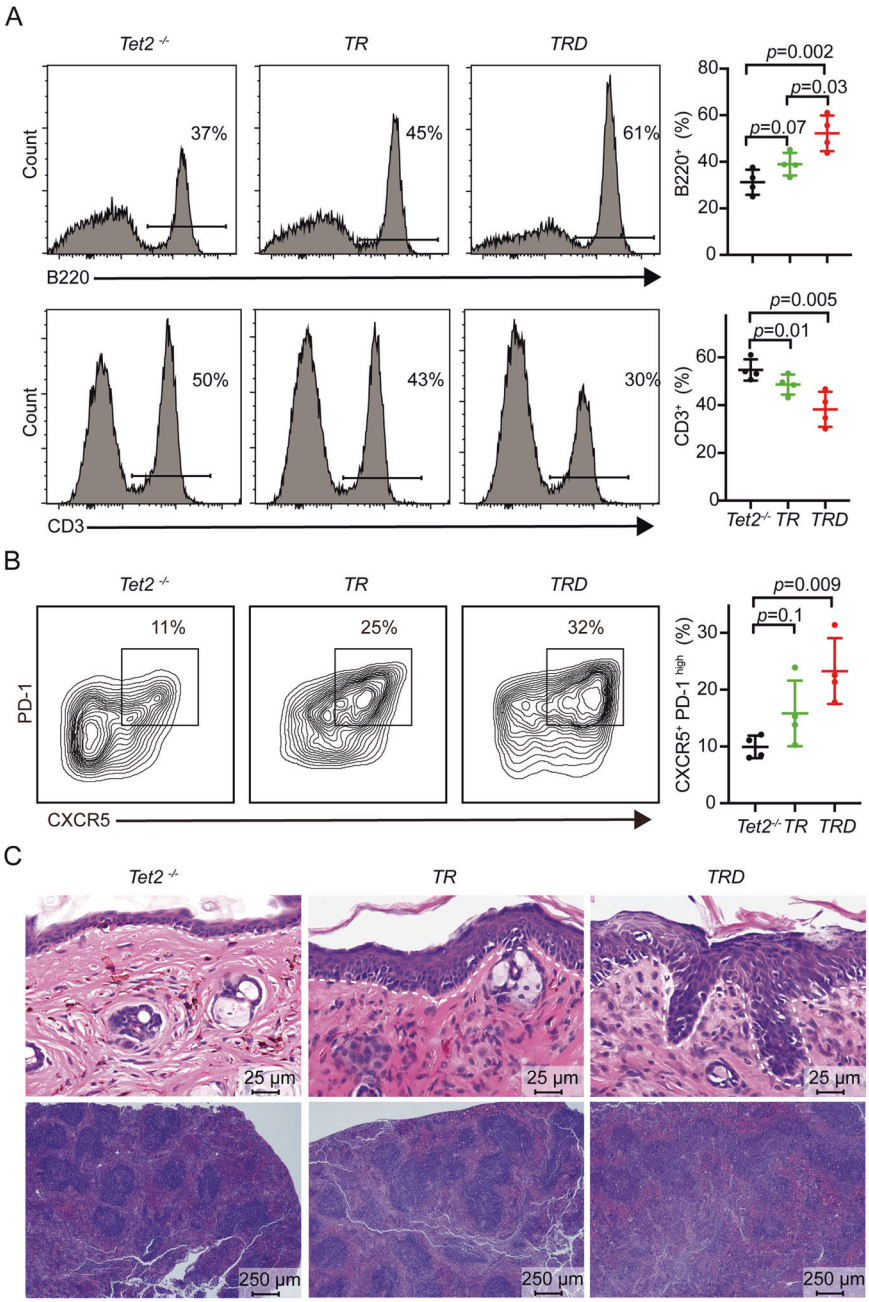

Fig. 3 ***DNMT3A*^{R882H} promotes the pathologic features of AITL. A** Flow cytometry analysis showing the CD3^{+}% T or B220^{+}% B cells in the lymph nodes of the *Tet2*$^{-/-}$, *TR*, and *TRD* recipients. means ± SD, $n = 4$. *P* value was obtained from a One-way ANOVA *t*-test. **B** Flow cytometry results showing the Tfh (CXCR5^{+} PD-1^{high} gated on CD4 +) population in the lymph nodes of the *Tet2*$^{-/-}$, *TR* and *TRD* groups along with the quantitation (means ± SD, $n = 4$; One-way ANOVA *t*-test). **C** Hematoxylin and Eosin (H&E) staining of the ear (upper) and spleen (lower) from the *Tet2*$^{-/-}$, *TR*, or *TRD* recipient mice.

recapitulated the Tfh-like phenotypes observed in patients with AITL and consistent with the previous findings [7, 15]. Hematoxylin and eosin (H&E) stainings of the *Tet2*$^{-/-}$, *TR*, and *TRD* mouse ears displayed severe autoinflammation associated with AITL-bearing *TRD* mice, like abnormal epidermal cell proliferation, fibrous tissue hyperplasia, and inflammatory cell infiltration extending from the skin into the underlying connective tissue and muscle (Fig. 3C). A more pronounced disruptive expansion of follicular structures was observed in the *TRD* spleens (Fig. 3C). The *TRD* lymph nodes were obliterated and primed with proliferative high endothelial venules and sufficient centroblasts and centrocytes (Ex. Fig. 2B), which were recognized as histopathological characteristics of AITL [24]. Immunohistochemistrical staining of the lymph nodes further showed an enlarged CD4^{+} compartment that simultaneously expressed PD-1 and BCL6 in the *TRD* group (Ex. Fig. 2C). Sequencing analysis of the TCR repertoire in the *TRD* spleen revealed the presence of monoclonal T cell populations in all cases analyzed (Ex. Fig. 2D). Given these results, we concluded that *DNMT3A*^{R882H} played an accelerating role in the AITL progression.

THE SINGLE-CELL LANDSCAPE OF AITL WITH *DNMT3A* MUTATION

To investigate the mechanisms of *DNMT3A*^{R882H} in AITL, we performed 10x Genomics' single-cell RNA sequencing of the lymph nodes harvested from the *Tet2*$^{-/-}$, *TR*, and *TRD* mice after

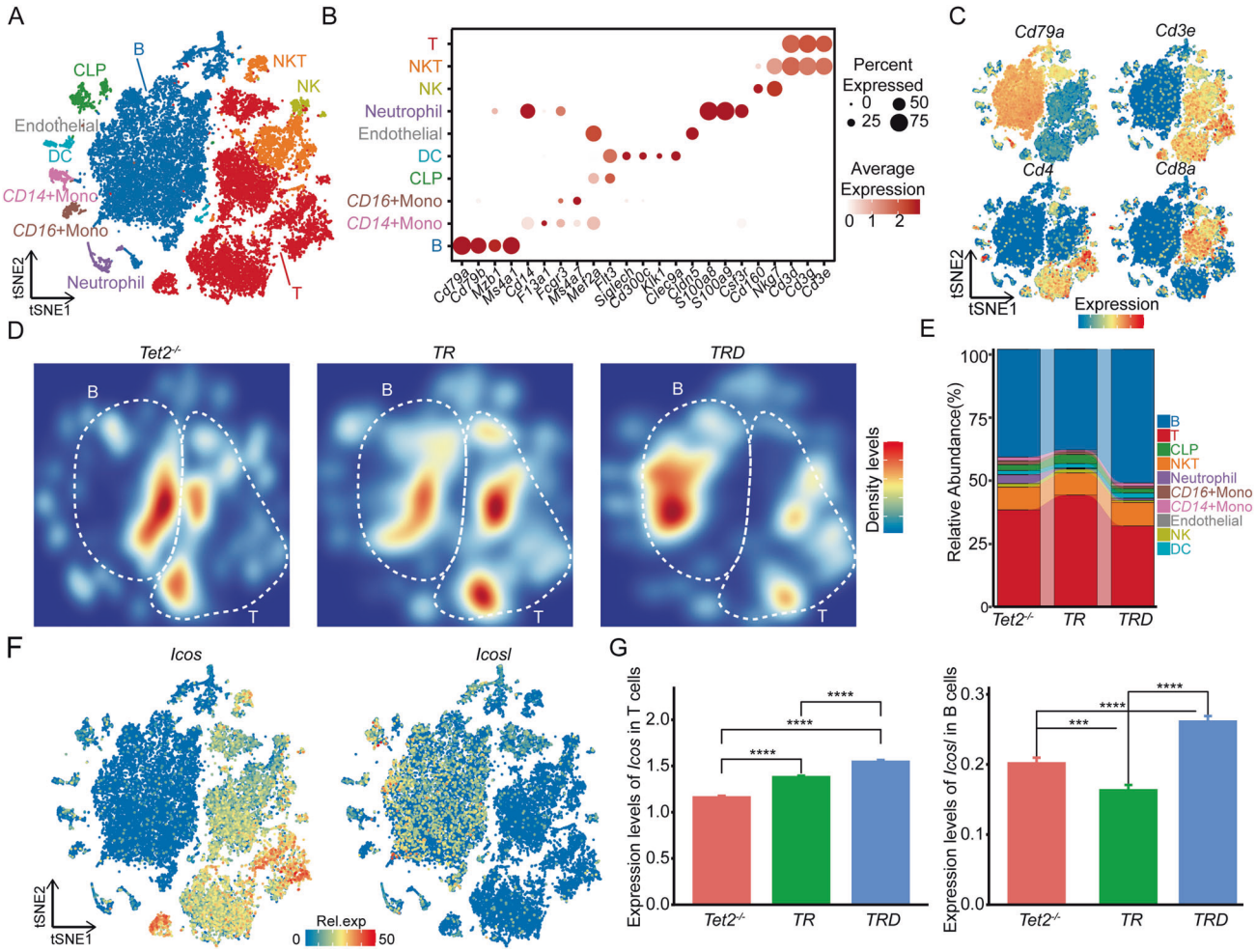

Fig. 4 The single-cell transcriptome analyses of mouse AITL. A The t-SNE map of single cell landscape of combined all cells from *Tet2*$^{-/-}$, *TR*, and *TRD* lymph nodes. **B** The dot plot showing the marker genes of each cell type. **C** The t-SNE maps showing the expression distributions of *Cd79a, Cd3e, Cd4*, and *Cd8a*. **D** The t-SNE density plots showing the sample origins from the *Tet2*$^{-/-}$, *TR*, and *TRD* lymph nodes. **E** The Alluvial plot showing the composition variation of cell populations in the *Tet2*$^{-/-}$, *TR*, and *TRD* lymph nodes. **F** The t-SNE maps showing the expression distributions of *Icos* and *Icosl*. **G** The bar plots showing the expression level of *Icos* and *Icosl* in the T cells and B cells of *Tet2*$^{-/-}$, *TR*, and *TRD* lymph nodes.

11 weeks of transplantation. The mitoQC maps showed that a total of 23,805 cells (7576 of *Tet2*$^{-/-}$, 7913 of *TR*, and 8316 of *TRD*) were used for clustering and further analysis (Ex. Fig. 3A) [25]. The t-SNE map displayed 10 populations that were identified by the classical gene's annotation, including 10,587 B cells (*Cd79a*, *Cd79b*, *Mzb1*, and *Ms4a1*), 279 CD14 + Monocytes cells (*Cd14* and *F13a1*), 263 CD16 + Monocytes cells (*Fcgr3* and *Ms4a7*), 591 common lymphocyte progenitor cells (*Mef2a* and *Flt3*), 413 dendritic cells (*Siglech*, *Cd300c*, *Klk1*, and *Clec9a*), 32 endothelial cells (*Cldn5*), 341 neutrophil cells (*S100a8*, *S100a9*, and *Csf3r*), 288 NK cells (*Cd160* and *Nkg7*), 2095 NKT cells (*Cd3e*, *Cd160*, and *Nkg7*) and 8916 T cells (*Cd3d*, *Cd3g*, and *Cd3e*) (Fig. 4A–B and Supplementary Table 7) [26, 27]. Besides, the expression levels of *Cd79a*, *Cd3e*, *Cd4*, and *Cd8a* were projected on the t-SNE map indicating the T cell and B cell distributions (Fig. 4C). Intriguingly, the distribution and proportion of T cells and B cells were largely shifted from *Tet2*$^{-/-}$, *TR* to *TRD* lymph nodes (Fig. 4D-E and Ex. Fig. 3B). In addition, the *Icos* was mostly expressed in T cells while *Icosl* was expressed mainly in B cells. The expression levels of both *Icos* and *Icosl* are significantly upregulated in *TRD* samples compared to that in *Tet2*$^{-/-}$ or *TR* groups (Fig. 4F–G), suggesting the formation and progression of AITL.

DNMT3A^{R882H} PROMOTES THE MALIGNANCIES OF TFH CELLS IN AITL

Given AITL is a T cell malignancy, we re-analyzed and annotated subpopulations of T cells among 10,069 NK/T cells based on the classical gene annotation. The force atlas map showed 15 subpopulations of T cells, including. 2848 *Lef1* + Naive. CD4T cells, 204 *Il17a* + Th17 cells, 276 *Il17f* + Th17 cells, 814 *Tnfrsf4* + Treg cells, 705 *Tnfsf8* + Tfh cells, 321 *Mki67* + Tfh cells, 616 Naive. CD8 T cells, 215 *Mif* + CD8 Tm cells, 1715 *Klrd1* + CD8 Tem cells, 1055 *Ly6c2* + CD8 Tem, 422 *Ifit1* + CD8 Tem cells, 180 *Eomes* + Tm cells, 213 *Nkg7* + NKT cells, 59 *Klrb1b* + NK cells and 426 *Xcl1* + NK cells (Fig. 5A). The top upregulated genes in T cells subpopulations were highlighted in the heatmap (Ex. Fig. 4A and Supplementary Table 8). The expression levels of naïve signatures, early-activation signatures, effector memory signatures, and exhausted signatures were projected on the force atlas map (Fig. 5B). Most of the T cells stayed in naïve status, but the NKT and MKI67 + Tfh cells kept active (Fig. 5B).

The origin and proportion of T cells were summarized on the force atlas map (Fig. 5C and Ex. Fig. 4B). Of note, the unceasing increase of Naïve CD8 T and *Ly6c2* + CD8 Tem cells were observed in *TRD* cells (Fig. 5C). And the Naïve CD8 T had the highest naïve

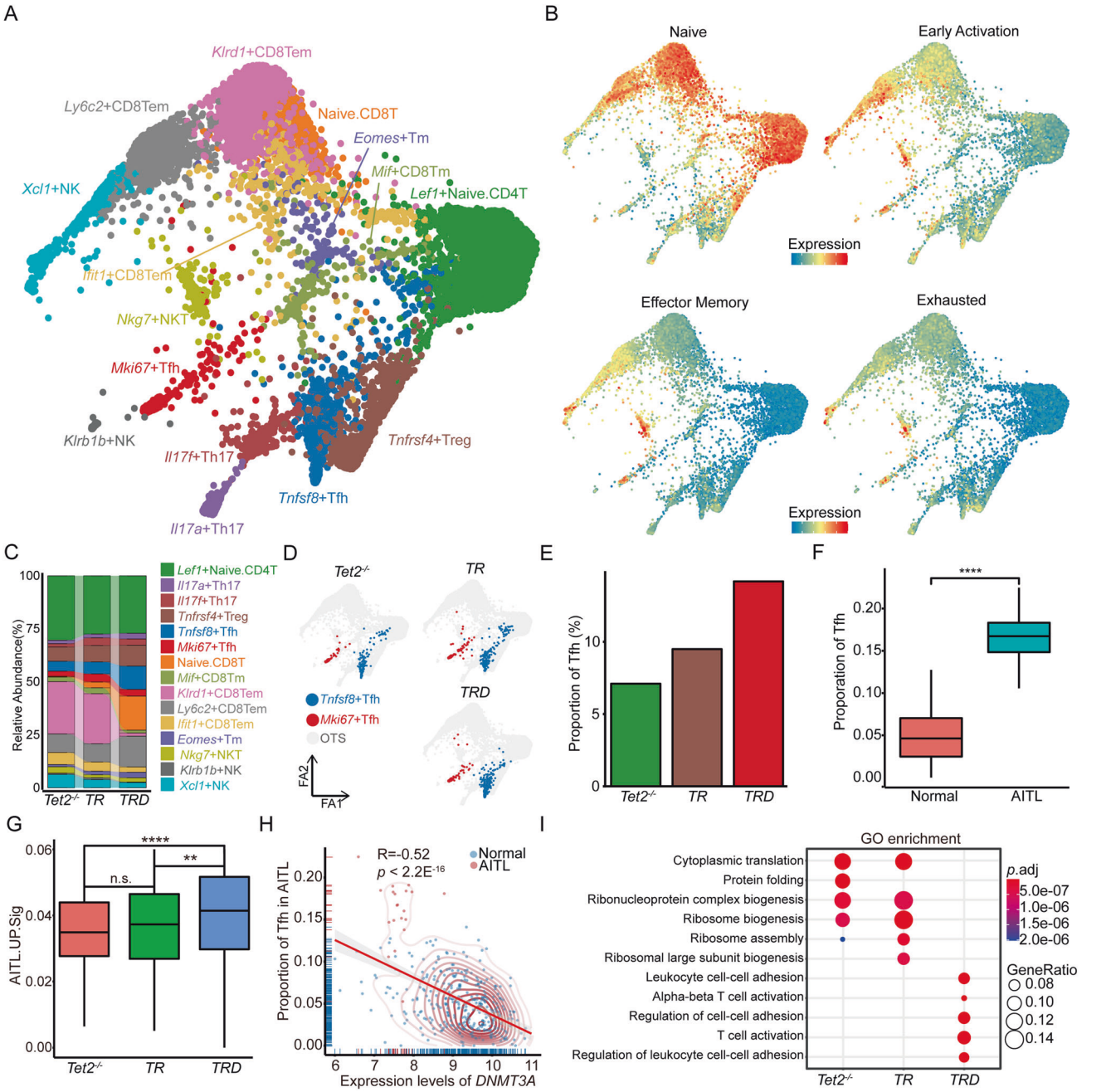

Fig. 5 ***DNMT3A*** ^{R882H} **promotes the activation of Tfh cells. A** The ForceAtlas2 maps showing the single-cell landscape of all T cells from *Tet2*$^{-/-}$, *TR*, and *TRD* lymph nodes. **B** The ForceAtlas2 maps showing the expression distributions of naïve, early activation, effector-memory, and exhausted signatures. **C** The Alluvial plot showing the composition variation of T cells in *Tet2*$^{-/-}$, *TR* or *TRD* lymph nodes. **D** The ForceAtlas2 plots showing the Tfh cells data from the *Tet2*$^{-/-}$, *TR* or *TRD* lymph nodes. **E** The bar plot showing the composition variation of Tfh in the *Tet2*$^{-/-}$, *TR* or *TRD* lymph nodes. **F** The boxplot showing the estimated proportion of Tfh in normal samples or AITL patients. **G** The boxplot showing the AITL up-regulated signatures in Tfh from *Tet2*$^{-/-}$, *TR* or *TRD* lymph nodes. **H** The boxplot showing the estimated proportion of Tfh in normal samples or AITL patients. The dot plot showing the top 5 enriched pathways of the GO biology process in Tfh from *Tet2*$^{-/-}$, *TR* or *TRD* lymph nodes.

scores, while the *Ly6c2* + CD8 Tem had the highest exhausted scores compared to other CD8 T cells, suggesting CD8 T cell's dysfunction (Ex. Fig. 4C). Of note, Tfh cells were dramatically increased in *TR* and *TRD* lymph nodes compared with *Tet2*$^{-/-}$ control, and were most enriched in *TRD* mice (Figs. 5D and 5E). Consistently, Tfh cells were also significantly enriched in AITL patients (Fig. 5F). Further, the Tfh cells from *TRD* mice had significantly upregulated expressions of genes involved in AITL_UP. Sig, TCR signaling, T cell activation, and lymphocyte differentiation (Fig. 5G and Ex. Fig. 4D). These results suggested that the *DNMT3A* mutation may alter T cell composition and promote the transformation of Tfh cells in AITL.

To check the correlation between *DNMT3A* and the Tfh cells in AITL patients, we deconvoluted the cell composition of AITL patients regarding the sc-RNA data as references. As Fig. 5H shows, a significant negative correlation between the expression of *DNMT3A* and the proportion of Tfh cells was observed (Supplementary Table 9). Most dots representing AITL patients

stayed in the upper left corner of the scatter plot, indicating a lower expression level of *DNMT3A* and a higher proportion of Tfh cells, compared with dots of the normal samples located in the lower right corner (Fig. 5H). The gene ontology (GO) biology process database was used to annotate the features of Tfh. The results showed that the Tfh population in *Tet2*$^{-/-}$ and *TR* lymph nodes had significantly enriched expressions of genes in ribosomal biogenesis and protein translation-related pathways, but the Tfh cells from *TRD* lymph nodes had significantly enriched T cell activation and cell-cell adhesion-related pathways (Fig. 5I, Supplementary Table 10, and Supplementary Table 11). These results suggested the *DNMT3A* mutation may stimulate the T cell activation and cell-cell interaction, especially enhancing the expansion and hyperactivity of Tfh cells.

DNMT3A^{R882H} ACCELERATES THE MATURATION OF B CELLS IN AITL

Given one of the pathology features of AITL is that B cells would largely expand in the lymph node, a total of 10,587 B cells were extracted and analyzed. Four major subpopulations of B cells were identified according to the classical genes' annotation, including 888 dark zone B cells (DZ. B cells), 3888 Memory B cells (Mem. B cells), 5643 precursor Memory B cells (preMem. B cells), and 168 plasma cells (Fig. 6A). These B cells could also be classified into 14 subpopulations, including 297 *Aicda* + DZ. B, 798 *Egr1* + preMem. B, 1324 *Ets1* + Mem. B, 534 *Fcrl5* + preMem. B, 734 *Hspa1a* + Mem. B, 1373 *Hspa1b* + preMem. B, 193 *Lars2* + Mem. B, 1237 Mem. B, 591 *Mki67* + DZ. B, 876 *Ncl* + preMem. B, 2062 preMem. B, 20 *Rag1* + Mem. B, 168 *Slpi* + plasma and 380 *Zbp1* + Mem. B (Fig. 6B, Ex. Figs. 5A and 5B Supplementary Table 12). Further, we found that B cells from *TRD* lymph nodes showed upregulated expressions of genes involved in B cell activation, immunoglobin production, and immunoglobin secretion (Ex. Fig. 5C). In addition, have higher AITL-UP.Sig scores were associated with the B cells from *TRD* mice, compared to the other two groups (Ex. Fig. 5D).

To investigate the impact of *DNMT3A*^{R882H} on B cells of AITL, we summarized the distributions and proportions of B cells and constructed the development trajectory of B cells based on RNA velocity (Fig. 6A). Of note, the lineage development of B cells in *Tet2*$^{-/-}$, *TR*, and *TRD* lymph nodes were distinguishable (Fig. 6C). More differentiated memory B cells were significantly enriched in *TR* and *TRD* B cells compared to that in *Tet2*$^{-/-}$ samples (Fig. 6C). Especially, Mem. B, *Ets1* + Mem. B and *Hspa1a* + Mem. B cells were significantly increased in *TRD* mice compared with others (Fig. 6B), suggesting that B cells from *TRD* lymph nodes were more active and differentiated. Moreover, four dynamics expression gene modules were identified based on the development trajectory of B cells (Fig. 6C). Among them, genes in module 4 were significantly upregulated on the terminal region in B cells' development trajectory of *TRD* lymph nodes. The GO biology process annotation of each module displayed that the IgG production and secretion-related pathways were significantly enriched in module 4 (Fig. 6D and Supplementary Table 13). Interestingly, the GO annotations also showed different cytokine-related pathways enriched in modules, such as response to interleukin-7 pathway in module 1, response to IL-4 pathway in module 2, IL-6/IL-12 production pathway in module 3, and IL-2 biosynthetic process in module 4 (Fig. 6D). These results reflected the function of B cells in different stages.

DNMT3A^{R882H} STRENGTHENS THE CROSSTALK BETWEEN TFH AND B CELLS IN AITL

We also investigated the interactions between Tfh and B cells in our AITL models. After the extrinsic interaction had been calculated and estimated by CellChat, the interaction signaling of CD86, MHC-II, ICAM, PDL1, and ICOS-related pathways were significantly upregulated in *TRD* samples compared with others (Ex. Fig. 6A–B). To illustrate the regulation between Tfh cells and B cells more clearly, the chord diagrams were used to visualize the specific interaction signaling (Fig. 6E and Ex. Fig. 6C). More B cell subpopulations showed the crosstalk with the Tfh cells from *TRD* lymph nodes compared to those in *Tet2*$^{-/-}$ or *TR* cells. The *Ncl* + preMem. B cells specifically interacted with Tfh in the *TRD* sample through PD-L1 interaction signaling. Besides PD-L1, CD86 and ICOS signaling, we also noticed that ICAM signaling was involved in the crosstalk between Tfh cells and various B subpopulations (Fig. 6E and Ex. Fig. 6C). Immunohistochemistry staining confirmed the increased ICAM1, PD-1, and CD86 levels in *TRD* lymph nodes (Ex. Fig. 7A).

To validate the interaction between Tfh cells and B cells in human AITL, we performed the scRNA-seq to analyze an AITL patient (GSE197188). A total of 2380 cells are collected and 9 populations have been identified by classical genes annotation (Ex. Fig. 7B). We found that the *CD86*, encoding a ligand, was specifically expressed in some B cells (Fig. 6F); *ICOSLG*, a ligand gene of ICOS interaction signaling, was specifically expressed in almost all B cells (Fig. 6F); *CD274*, encoding PD-L1, was mostly expressed in B cells (Ex. Fig. 7C); In contrast, *ICAM1*, a ligand gene of ICAM interaction signaling, was simultaneously expressed in both B cells and T cells (Ex. Fig. 7C). These expression patterns were consistent with those observed in TRD mice. Of note, the expression levels of *DNMT3A* were also negatively correlated with the expression levels of *CD86* and *ICOSLG* in AITL cohorts (Fig. 6G) [28]. These results suggested that *DNMT3A*^{R882H} strengthened the crosstalk between Tfh cells to B cells not only through known PD-L1, ICOS, and CD86 signaling but also through ICAM interaction signaling.

DISCUSSION

DNA methylation alteration is regarded as a crucial hallmark of cancer that exists in multiple cancer types and contributes to malignant transformation. The key guardians of DNA methylation, such as *TET2* (~30% and ~80%), *DNMT3A* (~25% and ~30%), and *IDH2* (~20% and ~30%) are frequently mutated in AML and AITL [11, 13, 18, 29–33]. These mutations have been validated as drivers in AML and other malignancies [34–37]. However, their roles in AILT are less studied. It has been demonstrated that *TET2* loss, cooperating with *RHOA*^{G17V}, drove AITL formation in mice [7]. Here, we found that *DNMT3A*^{R882H} mutant further promoted the progression of this disease in mice, demonstrated by increased malignant Tfh cell and abnormal B cell populations, enlarged lymph nodes, obvious skin rash, and shortened survival, all of which faithfully phenocopied those in the AITL patients. These results validated *DNMT3A* mutations as a driver of AITL. Previously it has been shown that *DNMT3A* and *TET2* mutations could cooperate to instigate leukemia [21], diverging from typical AITL as we reported here. This discrepancy might be explained by the incorporation of *RHOA*^{G17V} in our model, which is a defining mutation in AITL. *RHOA*^{G17V} could induce the specification of CD4^{+} T cells into Tfh cells with increased ICOS expression [7]. The combination of *RHOA*, *TET2*, and *DNMT3A* mutations happens in a large portion of AITL patients, and thus our model might represent the pathology of this disease. However, we noticed that in a previous study, 5 out of 18 mice transplanted with *Tet2* loss and *DNMT3A* ^{R882H} bone marrow cells developed AITL-like phenotypes [21]. And during the revision of our manuscript, it was reported that *IDH2*^{R172K} synergized with *TET2* loss to drive an AITL phenotype [38]. *IDH2*^{R172K} can also affect DNA methylation and other epigenetic regulation through its oncometabolite, 2-hydroxyglutarate [37, 39–41]. These studies, along with ours, underscore the importance of DNA methylation in AITL. Given that *DNMT3A*, *IDH2*, and *TET2* play different roles in DNA methylation

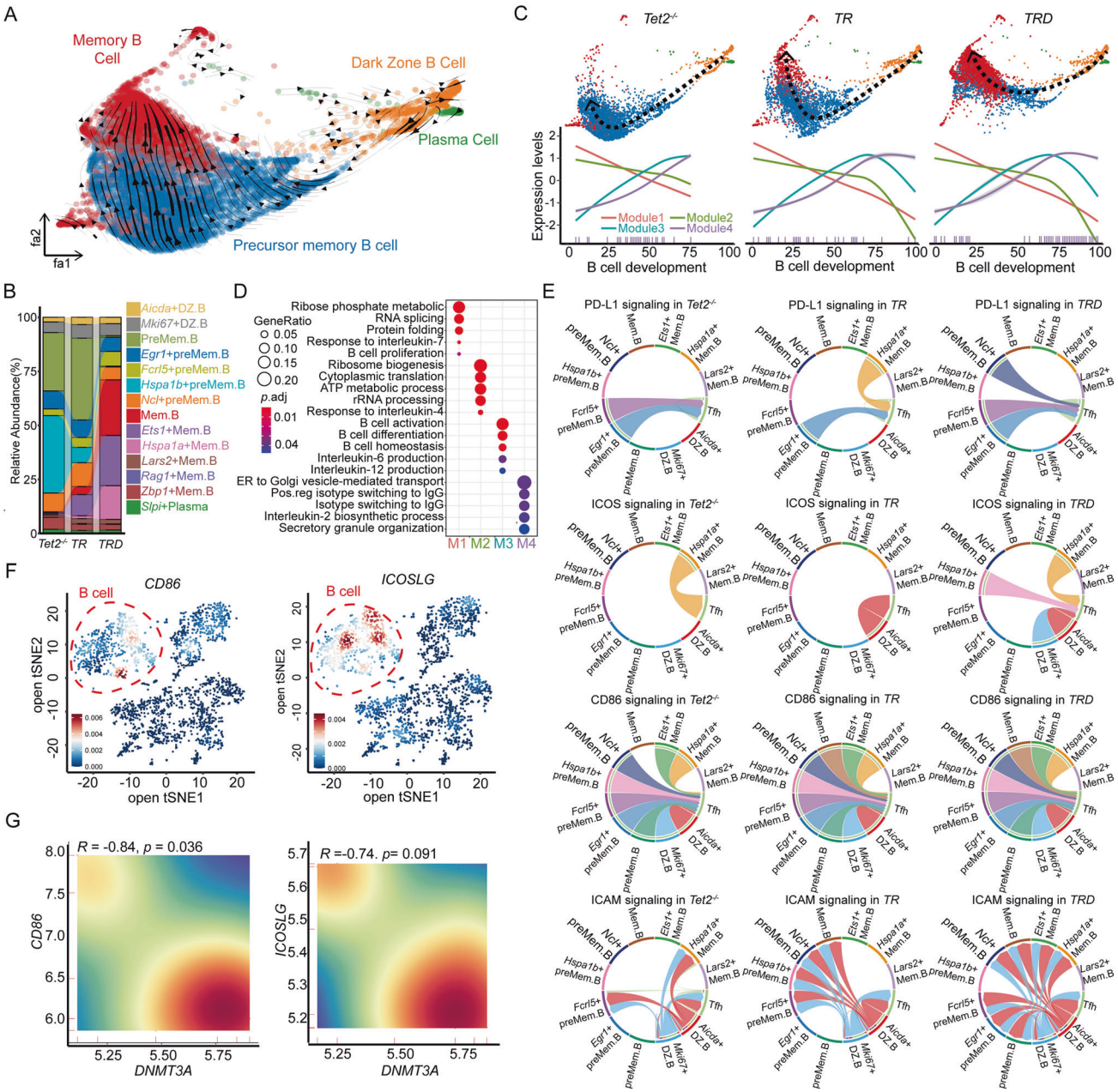

Fig. 6 Enhanced B cell differentiation and maturation in AITL mice with *DNMT3A* mutation. A The ForceAtlas2 maps showing the single-cell landscape of all B cells from *Tet2*$^{-/-}$, *TR*, and *TRD* lymph nodes. **B** The Alluvial plot showing the composition variation of the B cells subpopulation in *Tet2*$^{-/-}$, *TR* or *TRD* lymph nodes. **C** The ForceAtlas2 plots showing the B cells data from *Tet2*$^{-/-}$, *TR* or *TRD* lymph nodes (top). Dynamically expressed gene modules on the B cells development trajectory are present at the bottom. The bottom density dots showing the distribution of module 4 genes. **D** The dot plot showing the top 5 enriched pathways of the GO biology process in each module. **E** Chord plots showing the PD-L1, ICOS, CD86 or ICAM signaling in Tfh and various B subpopulations. **F** The openTSNE plots showing the expression and density distribution of *CD86* or *ICOSLG* in AITL patients. **G** The density plot showing the correlation between the expression levels of *DNMT3A* and *CD86* or *ICOSLG* in AITL patients.

and demethylation, their cooperation in AITL is striking. It would be fascinating to investigate the molecular mechanisms of these synergies.

AITL is an enigmatic malignancy, in terms of its complicated immune features besides the tumor cells. In this study, we dissected the cellular and molecular features of *DNMT3A*^{R882H} AITL, compared to *Tet2* loss, and *Tet2* loss plus *RHOA*^{R17V} mice, by single cell transcriptomics assay. Our data not only revealed the malignant progression of the Tfh cells driven by *RHOA* and *DNMT3A* mutations but also their interactions with the environmental cells, especially the B cells. We found that B cells were accelerated for maturation and showed super-activated features in the *DNMT3A*^{R882H} AITL mice. It has been proposed that the ICOS-ICOSL interaction between Tfh and B cells might be critical for AITL development [7]. Our data confirmed this interaction and *DNMT3A* mutation promoted the progression of AITL possibly through enhancing this interaction. Our analyses also revealed many other molecular interactions between the Tfh and B cells in AITL, including PD1/PD-L1, CD28/CD86, and ICAM1/ITGAL. It is notable that it has been shown that the B cells in AITL patients also contained *TET2* mutations [42]. And these *Tet2* mutant B cells might provide a niche for malignant T cells [43]. In our model, the

B cells derived from the transplanted bone marrow cells were also deficient in *Tet2*, which might also contribute to the pathology, just like those in patients. Future studies are needed to validate the functions of these interactions between the malignant Tfh cells and others, especially B cells, in AITL, and, more importantly, to explore their diagnostic and therapeutic values for AITL patients.

MATERIALS AND METHODS

Plasmid constructs

HEK-293T total RNA was extracted by guanidinium thiocyanate-phenol-chloroform extraction (TriZol, Applied Biosystems, Cat# 15596026) and used for cDNA synthesis with oligo dT mixed with random primers and the SuperScript II Reverse Transcriptase Kit (Invitrogen, Cat. No. 18064) following the manufacturer's protocol. Full-length human cDNA sequences of *RHOA* and *DNMT3A* were PCR amplified from the cDNA library and cloned into the pMSCV-IRES-GFP and pMSCV-IRES-mCherry retroviral vectors, respectively. Site-directed mutagenesis was performed to introduce the pGly17Val (G17V) and pArg882His (R882H) mutations.

Retroviral production and infection

To generate infectious retroviral particles, we co-transfected pMSCV-IRES-GFP, pMSCV-*RHOA*^{G17V}-IRES-GFP, pMSCV-IRES-mCherry or pMSCV-*DNMT3A*^{R882H}-IRES-mCherry retroviral constructs, along with p-Cleo and V-SVG viral packaging vectors, into HEK293T cells. The virus-containing supernatants were collected at 48- and 72-hours post-transfection and used to infect mouse bone marrow HSPCs by spinoculation.

Mice

All mouse experiments were approved by the Institutional Animal Care and Use Committees of Sichuan University. *Tet2*$^{-/-}$ mice were obtained from Jackson Laboratory (Cat: 023359). HSPCs were isolated from the femurs and tibia of 6 to 8-week-old *Tet2*$^{-/-}$ mice using anti-mouse CD117/c-Kit MicroBeads (cat. 130-091-224; Miltenyi Biotec) and an autoMACS machine (Miltenyi Biotec) following the manufacturer's instructions. Purified HSPCs were cultured in BCM medium 40% DMEM, 40% IMDM, 20% FBS, 50 μM β-Mercaptoethanol, penicillin (100 U/mL)/streptomycin (0.1 mg/mL) 5 ng/ml IL-3(cat. 403-ML-050; R&D), 50 ng/ml IL-6 (cat. 406-ML-025; R&D) and 50 ng/ml SCF (cat. 455-MC-050; R&D) at 37 °C with 7.5% CO2. For in vivo tumorigenesis, enriched *Tet2*$^{-/-}$ HSPCs were transduced with retroviruses carrying *RHOA*^{G17V}-IRES-GFP only (*TR*), or together with *DNMT3A*^{R882H}-IRES-mCherry (*TRD*), or empty vector (*Tet2*$^{-/-}$), respectively, and injected intravenously into sub-lethally irradiated (5.5 Gray) male C57BL/6 recipient mice (6–8 weeks old, $1 \times 10\text{^}6$ each, $n = 4$–8 each group). All recipient mice were randomly divided into different groups before transplantation and were monitored once per week by palpation. The tumor monitoring process was performed by a blinded method. The immunophenotypes of the resulting AITL were analyzed by flow cytometry using antibodies purchased from Invitrogen. Survival data were analyzed using the log-rank test from GraphPad Prism 8.

Flow cytometry

Total white blood cells, obtained from peripheral blood after lysis of red blood cells, and single-cell suspensions from bone marrow, spleen and lymph node were stained with fluorochrome-conjugated mouse antibodies raised against specific markers (Invitrogen, except otherwise mentioned) in PBS supplemented with 2% fetal bovine serum (FBS). Flow cytometry analyses were conducted on the BD LSRFortessa™ Flow Cytometer (BD Biosciences, San Jose, CA) and immunophenotypic data were analyzed using FlowJo Version 10.8.1 software (Ashland, OR) [14]. Antibodies used in flow cytometry are displayed in Supplementary Table 14.

Histopathology and immunohistochemistry

Spleen, ear and lymph nodes were fixed in 4% paraformaldehyde (PFA) and sections were stained with Hematoxylin and Eosin (H&E). In terms of immunohistochemistry (IHC), primary antibodies were diluted at a 1:50-1:500 dilution in 2% goat serum and incubated overnight at 4 °C. A two-step detection kit (PV-9001 and PV-9002) was used for IHC, and hematoxylin was used for nuclear staining. Antibodies used in IHC are displayed in Supplementary Table 15.

T cell receptor variable beta chain (TCR Vβ) repertoire analysis

TCR Vβ repertoire analysis of RNA samples by high throughput sequencing was performed at Chengdu ExAb Biotechnology (Chengdu, China) using Ion GeneStudio S5 system (Thermo fisher, USA). Data obtained by high throughput sequencing was analyzed with IRIS (Immune Receptor Information System) software [44]. Clonal expansion was assessed by comparing of the TCR Vβ repertoire distribution in splenic donor cells in *TRD* groups.

Single-cell RNA-seq analysis

Lymph nodes were collected from the *Tet2*$^{-/-}$ ($n = 3$), *TR* ($n = 1$), and *TRD* ($n = 1$) groups and washed with PBS supplemented with 2% fetal bovine serum (FBS). The ground lymph node tissue was filtered through a 100um filter to obtain a single-cell suspension. Cell numbers were quantified, and the concentration was adjusted to 800–1200 cells/μl, with a cell activity >85%. Single-cell suspensions were subjected to single-cell RNA sequencing (scRNA-seq) within an hour of acquisition, using the 10X genomics platform to construct the single-cell library of samples.

The Biomarker Technologies Corporation provided the service of library preparation and sequencing of scRNA-seq data (www.biomarker.com.cn and www.biocloud.net). The 10X genomics platform was used to prepare the library with Chromium Single Cell 3' Reagent Kits v3, following the manufactory's protocol. Paired-end 150 bp sequencing was performed on an Illumina NovaSeq 6000 for each sample. The cellranger (v5.0.1) was used to align the clean reads with the mm10 genome reference. The Seurat (v3.2.3) pipeline was used to quantify and visualize single-cell RNA data. Poor-quality cells with detectable gene numbers lower than 200 or higher than 7500 were removed, as well as poor-quality genes detected less than 3 cells. MiQC (v1.1.5) was used to perform quality control on each sample with the spline model, with posterior_cutoff = 0.75. A total of 23,805 cells were finally harvested, with 7913 cells detected in *Tet2*$^{-/-}$ samples, 7576 cells in the *TR* lymph nodes, and 8316 cells in the *TRD* lymph nodes.

The vst model implemented in FindVariableFeatures was used to identify 4000 high-variable genes for subsequent processing. And the 30 PCA components were used for embedding calculation. The t-SNE and force atlas was used to reduce the dimension of scRNA-seq data following previously reported methods [26, 45]. Each subpopulation was identified by classical signatures [46], and top markers were calculated by FindAllMarkers.

The slingshot (v1.4.0) and RNA velocity were used to infer the B cells' development. The velocyto (v0.17.17) was used to calculate the spliced, unspliced and ambiguous counts in each sample. The velocyto. R (v0.6) and SeuratWrappers (v0.2.0) were used to convert the loom files into a seurat object. The scvelo (v0.2.4) was used to calculate and visualize the RNA velocity on the force atlas. Besides, the slingshot (v1.4.0) was used to confirm the B cells development lineage with 300 approximate points. The genSmoothCurves implemented in monocle (v2.14.0) was used to order cells based on the trajectory. The dynamics expression genes among the B cells development were identified by differentialGeneTest function, and the qval <1e^{-100} of candidate genes would be reminded.

Gene-sets enrichment and gene signatures identified

All the enrichment gene sets were downloaded from GSEA (v7 database), including PICCALUGA_ANGIOIMMUNOBLASTIC_LYMPHOMA_UP for AITL_UP.Sig quantification; GO_IMMUNOGLOBULIN_PRODUCTION, GO_IMMUNOGLOBULIN_SECRETION, GO_REGULATION_OF_B_CELL_RECEPTOR_SIGNALING_PATHWAY, and MORI_PLASMA_CELL_UP for immunoglobin production and secretion quantification; PID_CD8_TCR_DOWNSTREAM_PATHWAY, GO_LYMPHOCYTE_DIFFERENTIATION, and GO_REGULATION_OF_ALPHA_BETA_T_CELL_ACTIVATION for Tfh cells activation quantification. The clusterProfiler (v3.14.3) was used to annotate the GO biology process and KEGG database. And the GSEA implemented in clusterProfiler was used to enrich the HALLMARK pathways based on the ranked gene list generated from AITL versus normal samples and DNMT3A^{lo} versus DNMT3A^{hi} patients.

Omics data analysis of AITL database

The mutation of *RHOA*, *TET2*, and *DNMT3A* in AITL was collected from 39 patients of cohort 1, 30 patients of cohort 2, and 48 patients of cohort 3 [12, 13, 18, 20]. The transcriptome data were collected, including 6 AITL patients and 20 normal samples from GSE6338, 20 AITL patients from GSE51521, and 337 normal blood samples from GTEx [22]. The scRNA-seq data of AITL patients were collected from GSE197188.

Statistical analysis

Statistical test methods, sample sizes, and *p* values are indicated in the corresponding figure legends. Statistical analyses were performed using GraphPad Prism (RRID: SCR_002798; GraphPad Software). The log-rank test was used to compare survival differences among groups for the Kaplan–Meier disease-free survival curve. A one-way ANOVA *t*-test was used to determine the statistical significance and hypergeometric tests were used to determine *p* values for the Venn diagram overlap analysis. Box plots were generated using ggpubr, with the horizontal center lines denoting the median and box edges denoting the interquartile range. *P*adj was calculated by the Wilcoxon signed-rank test and adjusted by holm.

DATA AVAILABILITY

Single-cell RNA-seq data were deposited in the Gene Expression Omnibus database repository under accession number 142645. The private code of GSE142645 is mfuvgkuerburdqr.

CODE AVAILABILITY

The analysis code can be found on GitHub (https://github.com/pangxueyu233/DNMT3AR882H-accelerates-angioimmunoblastic-T-cell-lymphoma).

REFERENCES

1. Vose J, Armitage J, Weisenburger D. International peripheral T-cell and natural killer/T-cell lymphoma study: pathology findings and clinical outcomes. J Clin Oncol: Off J Am Soc Clin Oncol. 2008;26:4124–30. https://doi.org/10.1200/jco.2008.16.4558.
2. Mourad N, Mounier N, Brière J, Raffoux E, Delmer A, Feller A, et al. Clinical, biologic, and pathologic features in 157 patients with angioimmunoblastic T-cell lymphoma treated within the Groupe d'Etude des Lymphomes de l'Adulte (GELA) trials. Blood. 2008;111:4463–70. https://doi.org/10.1182/blood-2007-08-105759.
3. Federico M, Rudiger T, Bellei M, Nathwani BN, Luminari S, Coiffier B, et al. Clinicopathologic characteristics of angioimmunoblastic T-cell lymphoma: analysis of the international peripheral T-cell lymphoma project. J Clin Oncol: Off J Am Soc Clin Oncol. 2013;31:240–6. https://doi.org/10.1200/jco.2011.37.3647.
4. Attygalle AD, Kyriakou C, Dupuis J, Grogg KL, Diss TC, Wotherspoon AC, et al. Histologic evolution of angioimmunoblastic T-cell lymphoma in consecutive biopsies: clinical correlation and insights into natural history and disease progression. Am J Surg Pathol. 2007;31:1077–88. https://doi.org/10.1097/PAS.0b013e31802d68e9.
5. de Leval L, Rickman DS, Thielen C, Reynies A, Huang YL, Delsol G, et al. The gene expression profile of nodal peripheral T-cell lymphoma demonstrates a molecular link between angioimmunoblastic T-cell lymphoma (AITL) and follicular helper T (TFH) cells. Blood. 2007;109:4952–63. https://doi.org/10.1182/blood-2006-10-055145.
6. Piccaluga PP, Agostinelli C, Califano A, Carbone A, Fantoni L, Ferrari S, et al. Gene expression analysis of angioimmunoblastic lymphoma indicates derivation from T follicular helper cells and vascular endothelial growth factor deregulation. Cancer Res. 2007;67:10703–10. https://doi.org/10.1158/0008-5472.Can-07-1708.
7. Cortes JR, Ambesi-Impiombato A, Couronné L, Quinn SA, Kim CS, da Silva Almeida AC, et al. RHOA G17V induces T follicular helper cell specification and promotes lymphomagenesis. Cancer Cell. 2018;33:259–.e257. https://doi.org/10.1016/j.ccell.2018.01.001.
8. Chiba S, Sakata-Yanagimoto M. Advances in understanding of angioimmunoblastic T-cell lymphoma. Leukemia. 2020;34:2592–606. https://doi.org/10.1038/s41375-020-0990-y.
9. Mondragón L, Mhaidly R, De Donatis GM, Tosolini M, Dao P, Martin AR, et al. GAPDH overexpression in the T cell lineage promotes angioimmunoblastic T cell lymphoma through an NF-κB-dependent mechanism. Cancer Cell. 2019;36:268–.e210. https://doi.org/10.1016/j.ccell.2019.07.008.
10. Shi J, Hou S, Fang Q, Liu X, Liu X, Qi H. PD-1 controls follicular T helper cell positioning and function. Immunity. 2018;49:264–.e264. https://doi.org/10.1016/j.immuni.2018.06.012.
11. Odejide O, Weigert O, Lane AA, Toscano D, Lunning MA, Kopp N, et al. A targeted mutational landscape of angioimmunoblastic T-cell lymphoma. Blood. 2014;123:1293–6. https://doi.org/10.1182/blood-2013-10-531509.
12. Sakata-Yanagimoto M, Enami T, Yoshida K, Shiraishi Y, Ishii R, Miyake Y, et al. Somatic RHOA mutation in angioimmunoblastic T cell lymphoma. Nat Genet. 2014;46:171–5. https://doi.org/10.1038/ng.2872.
13. Palomero T, Couronné L, Khiabanian H, Kim MY, Ambesi-Impiombato A, Perez-Garcia A, et al. Recurrent mutations in epigenetic regulators, RHOA and FYN kinase in peripheral T cell lymphomas. Nat Genet. 2014;46:166–70. https://doi.org/10.1038/ng.2873.
14. FlowJo™ Software. Version 10.3. Ashland, OR: Becton, Dickinson and Company. 2019.
15. Ng SY, Brown L, Stevenson K, deSouza T, Aster JC, Louissaint A Jr., et al. RhoA G17V is sufficient to induce autoimmunity and promotes T-cell lymphomagenesis in mice. Blood. 2018;132:935–47. https://doi.org/10.1182/blood-2017-11-818617.
16. Ley TJ, Ding L, Walter MJ, McLellan MD, Lamprecht T, Larson DE, et al. DNMT3A mutations in acute myeloid leukemia. N. Engl J Med. 2010;363:2424–33. https://doi.org/10.1056/NEJMoa1005143.
17. Shah MY, Licht JD. DNMT3A mutations in acute myeloid leukemia. Nat Genet. 2011;43:289–90. https://doi.org/10.1038/ng0411-289.
18. Wang C, McKeithan TW, Gong Q, Zhang W, Bouska A, Rosenwald A, et al. IDH2R172 mutations define a unique subgroup of patients with angioimmunoblastic T-cell lymphoma. Blood. 2015;126:1741–52. https://doi.org/10.1182/blood-2015-05-644591.
19. Yao WQ, Wu F, Zhang W, Chuang SS, Thompson JS, Chen Z, et al. Angioimmunoblastic T-cell lymphoma contains multiple clonal T-cell populations derived from a common TET2 mutant progenitor cell. J Pathol. 2020;250:346–57. https://doi.org/10.1002/path.5376.
20. Nguyen TB, Sakata-Yanagimoto M, Asabe Y, Matsubara D, Kano J, Yoshida K, et al. Identification of cell-type-specific mutations in nodal T-cell lymphomas. Blood Cancer J. 2017;7:e516 https://doi.org/10.1038/bcj.2016.122.
21. Scourzic L, Couronné L, Pedersen MT, Della Valle V, Diop M, Mylonas E, et al. DNMT3A(R882H) mutant and Tet2 inactivation cooperate in the deregulation of DNA methylation control to induce lymphoid malignancies in mice. Leukemia. 2016;30:1388–98. https://doi.org/10.1038/leu.2016.29.
22. Crescenzo R, Abate F, Lasorsa E, Tabbo F, Gaudiano M, Chiesa N, et al. Convergent mutations and kinase fusions lead to oncogenic STAT3 activation in anaplastic large cell lymphoma. Cancer Cell. 2015;27:516–32. https://doi.org/10.1016/j.ccell.2015.03.006.
23. Lu KT, Kanno Y, Cannons JL, Handon R, Bible P, Elkahloun AG, et al. Functional and epigenetic studies reveal multistep differentiation and plasticity of in vitro-generated and in vivo-derived follicular T helper cells. Immunity. 2011;35:622–32. https://doi.org/10.1016/j.immuni.2011.07.015.
24. Attygalle A, Al-Jehani R, Diss TC, Munson P, Liu H, Du M-Q, et al. Neoplastic T cells in angioimmunoblastic T-cell lymphoma express CD10. Blood. 2002;99:627–33. https://doi.org/10.1182/blood.V99.2.627.
25. Hippen AA, Falco MM, Weber LM, Erkan EP, Zhang K, Doherty JA, et al. miQC: an adaptive probabilistic framework for quality control of single-cell RNA-sequencing data. PLOS Comput Biol. 2021;17:e1009290 https://doi.org/10.1371/journal.pcbi.1009290.
26. Na F, Pan X, Chen J, Chen X, Wang M, Chi P, et al. KMT2C deficiency promotes small cell lung cancer metastasis through DNMT3A-mediated epigenetic reprogramming. Nat Cancer. 2022;3:753–67. https://doi.org/10.1038/s43018-022-00361-6.
27. Wang M, Chen X, Tan P, Wang Y, Pan X, Lin T, et al. Acquired semi-squamatization during chemotherapy suggests differentiation as a therapeutic strategy for bladder cancer. Cancer Cell. 2022;40:1044–.e1048. https://doi.org/10.1016/j.ccell.2022.08.010.
28. Pritchett JC, Yang ZZ, Kim HJ, Villasboas JC, Tang X, Jalali S, et al. High-dimensional and single-cell transcriptome analysis of the tumor microenvironment in angioimmunoblastic T cell lymphoma (AITL). Leukemia. 2022;36:165–76. https://doi.org/10.1038/s41375-021-01321-2.
29. Yoo HY, Sung MK, Lee SH, Kim S, Lee H, Park S, et al. A recurrent inactivating mutation in RHOA GTPase in angioimmunoblastic T cell lymphoma. Nat Genet. 2014;46:371–5. https://doi.org/10.1038/ng.2916.
30. Cortes JR, Palomero T. The curious origins of angioimmunoblastic T-cell lymphoma. Curr Opin Hematol. 2016;23:434–43. https://doi.org/10.1097/MOH.0000000000000261.
31. Lemonnier F, Couronné L, Parrens M, Jaïs JP, Travert M, Lamant L, et al. Recurrent TET2 mutations in peripheral T-cell lymphomas correlate with TFH-like features and adverse clinical parameters. Blood. 2012;120:1466–9. https://doi.org/10.1182/blood-2012-02-408542.
32. Couronné L, Bastard C, Bernard OA. TET2 and DNMT3A mutations in human T-cell lymphoma. N. Engl J Med. 2012;366:95–96. https://doi.org/10.1056/NEJMc1111708.
33. Fukumoto K, Nguyen TB, Chiba S, Sakata-Yanagimoto M. Review of the biologic and clinical significance of genetic mutations in angioimmunoblastic T-cell lymphoma. Cancer Sci. 2018;109:490–6. https://doi.org/10.1111/cas.13393.
34. Li Z, Cai X, Cai CL, Wang J, Zhang W, Petersen BE, et al. Deletion of Tet2 in mice leads to dysregulated hematopoietic stem cells and subsequent development of myeloid malignancies. Blood. 2011;118:4509–18. https://doi.org/10.1182/blood-2010-12-325241.
35. Moran-Crusio K, Reavie L, Shih A, Abdel-Wahab O, Ndiaye-Lobry D, Lobry C, et al. Tet2 loss leads to increased hematopoietic stem cell self-renewal and myeloid transformation. Cancer Cell. 2011;20:11–24. https://doi.org/10.1016/j.ccr.2011.06.001.

36. Yang L, Rodriguez B, Mayle A, Park HJ, Lin X, Luo M, et al. DNMT3A loss drives enhancer hypomethylation in FLT3-ITD-associated leukemias. Cancer Cell. 2016;29:922–34. https://doi.org/10.1016/j.ccell.2016.05.003.
37. Chen C, Liu Y, Lu C, Cross JR, Morris JPT, Shroff AS, et al. Cancer-associated IDH2 mutants drive an acute myeloid leukemia that is susceptible to Brd4 inhibition. Genes Dev. 2013;27:1974–85. https://doi.org/10.1101/gad.226613.113.
38. Leca J, Lemonnier F, Meydan C, Foox J, El Ghamrasni S, Mboumba DL et al. IDH2 and TET2 mutations synergize to modulate T Follicular Helper cell functional interaction with the AITL microenvironment. Cancer Cell. 2023; https://doi.org/10.1016/j.ccell.2023.01.003.
39. Gross S, Cairns RA, Minden MD, Driggers EM, Bittinger MA, Jang HG, et al. Cancer-associated metabolite 2-hydroxyglutarate accumulates in acute myelogenous leukemia with isocitrate dehydrogenase 1 and 2 mutations. J Exp Med. 2010;207:339–44. https://doi.org/10.1084/jem.20092506.
40. Janin M, Mylonas E, Saada V, Micol JB, Renneville A, Quivoron C, et al. Serum 2-hydroxyglutarate production in IDH1- and IDH2-mutated de novo acute myeloid leukemia: a study by the acute leukemia French association group. J Clin Oncol. 2014;32:297–305. https://doi.org/10.1200/jco.2013.50.2047.
41. Chotirat S, Thongnoppakhun W, Promsuwicha O, Boonthimat C, Auewarakul CU. Molecular alterations of isocitrate dehydrogenase 1 and 2 (IDH1 and IDH2) metabolic genes and additional genetic mutations in newly diagnosed acute myeloid leukemia patients. J Hematol Oncol. 2012;5:5 https://doi.org/10.1186/1756-8722-5-5.
42. Schwartz FH, Cai Q, Fellmann E, Hartmann S, Mäyränpää MI, Karjalainen-Lindsberg ML, et al. TET2 mutations in B cells of patients affected by angioimmunoblastic T-cell lymphoma. J Pathol. 2017;242:129–33. https://doi.org/10.1002/path.4898.
43. Fujisawa M, Nguyen TB, Abe Y, Suehara Y, Fukumoto K, Suma S, et al. Clonal germinal center B cells function as a niche for T-cell lymphoma. Blood. 2022;140:1937–50. https://doi.org/10.1182/blood.2022015451.
44. Kelley J, de Bono B, Trowsdale J. IRIS: a database surveying known human immune system genes. Genomics. 2005;85:503–11. https://doi.org/10.1016/j.ygeno.2005.01.009.
45. Pan X, Wang J, Guo L, Na F, Du J, Chen X, et al. Identifying a confused cell identity for esophageal squamous cell carcinoma. Signal Transduct Target Ther. 2022;7:122 https://doi.org/10.1038/s41392-022-00946-8.
46. Liu P, Pan X, Chen C, Niu T, Shuai X, Wang J, et al. Nivolumab treatment of relapsed/refractory Epstein-Barr virus-associated hemophagocytic lymphohistiocytosis in adults. Blood. 2020;135:826–33. https://doi.org/10.1182/blood.2019003886.

ACKNOWLEDGEMENTS

We thank all the members of the Chen and Liu laboratory for their invaluable suggestions and technical support. We thank Dr. Yuquan Wei for his generous support. We thank Dr. Renzhan Tong for his technical support. We thank the Core Facilities of West China Hospital for technical support.

AUTHOR CONTRIBUTIONS

CC and YL conceived the project and designed experiments. ZW, JZ, ZZ, HL, PL, QZ, XD and FN performed experiments. XP performed bioinformatic analyses. ZW, JZ, XP, CC, TN and YL analyzed data. ZW, JZ, XP, TN and YL prepared and wrote the manuscript. All authors read and approved the final manuscript.

FUNDING

This work was supported by the National Natural Science Foundation of China (82130007), the Sichuan Science and Technology Program (2018RZ0140, 2018JZ0077, 2022YFS0205), the Incubation Program for Clinical Trials (19HXFH030), the Achievement Transformation Project (CGZH21001), the 1.3.5 Project for Disciplines of Excellence, West China Hospital, Sichuan University (ZYJC21009, ZYGD22012, ZYJC21007), and the Translational Research Grant of NCRCH (2021WWB03).

COMPETING INTERESTS

The authors declare no competing interests.

ADDITIONAL INFORMATION

Supplementary information The online version contains supplementary material available at https://doi.org/10.1038/s41388-023-02699-2.

Correspondence and requests for materials should be addressed to Ting Niu or Yu Liu.

Reprints and permission information is available at http://www.nature.com/reprints

Publisher's note Springer Nature remains neutral with regard to jurisdictional claims in published maps and institutional affiliations.